

Deep optical observations contemporaneous with emission from the periodic FRB 180916.J0158+65

CHARLES D. KILPATRICK,¹ JOSEPH N. BURCHETT,² DAVID O. JONES,³ BEN MARGALIT,⁴ RUSSET MCMILLAN,⁵ WEN-FAI FONG,¹
KASPER E. HEINTZ,⁶ NICOLAS TEJOS,⁷ AND ALICIA ROUCO ESCORIAL¹

¹*Center for Interdisciplinary Exploration and Research in Astrophysics (CIERA) and Department of Physics and Astronomy, Northwestern University, Evanston, IL 60208, USA*

²*Astronomy Department, Box 30001, Department 4500, New Mexico State University, Las Cruces, NM 88003-0001*

³*Department of Astronomy and Astrophysics, University of California, Santa Cruz, CA 95064, USA*

⁴*Astronomy Department and Theoretical Astrophysics Center, University of California, Berkeley, Berkeley, CA 94720, USA*

⁵*Apache Point Observatory and New Mexico State University, P.O. Box 59, Sunspot, NM, 88349-0059, USA*

⁶*Centre for Astrophysics and Cosmology, Science Institute, University of Iceland, Dunhagi 5, 107 Reykjavík, Iceland*

⁷*Instituto de Física, Pontificia Universidad Católica de Valparaíso, Casilla 4059, Valparaíso, Chile*

ABSTRACT

We present deep Apache Point Observatory optical observations within seconds of the outburst of the periodic fast radio burst (FRB) 180916.J0158+65 obtained on 3 September 2020. FRB 180916.J0158+65 is located in a nearby spiral galaxy 150 Mpc away and has an “active phase” with a well-measured period of approximately 16.3 days. Targeting the FRB at the peak of its expected active phase and during a recent 30 minute observing window by the Canadian Hydrogen Intensity Mapping Experiment (CHIME) in which a radio burst was detected, we did not detect any transient optical emission at $m_i \approx 24.7$ mag (3σ) from 2.2 to 1938.1 seconds after the burst arrival time in optical bands (corrected for dispersion). Comparing our limiting magnitudes to models of a synchrotron maser formed in the circumburst environment of FRB 180916+J0158.65, we constrain scenarios where the burst energy was $> 10^{44}$ erg and the circumburst density was $> 10^4$ cm⁻³.

1. INTRODUCTION

Fast radio bursts (FRBs) are millisecond timescale (Lorimer et al. 2007) bursts of MHz–GHz radio emission from extragalactic sources (Thornton et al. 2013; CHIME/FRB Collaboration et al. 2019; Cordes & Chatterjee 2019; Petroff et al. 2019a, and references therein). The detection of the first repeating FRB 121102 (Spitler et al. 2014, 2016) enabled its precise localization in a host galaxy at $z = 0.193$ (Chatterjee et al. 2017). There may also be a non-repeating population of FRBs (e.g., Ai et al. 2020; Hashimoto et al. 2020), but the observed FRB rate and luminosity function suggests that most of these sources must be repeating (whether or not they are observed to repeat, e.g., Ravi et al. 2019; Caleb et al. 2019). A handful of these FRBs with multiple detections have been accurately localized and securely associated with host galaxies, spanning a wide range of host types from star forming (FRB 121102 and FRB 190711; Chatterjee et al. 2017; Macquart et al. 2020; Li & Zhang 2020; Kumar et al. 2020) to quiescent (FRB 180916 and FRB 180924 with a star-formation rate $< 2 M_{\odot} \text{ yr}^{-1}$

at $z = 0.3214$; Bannister et al. 2019; Marcote et al. 2020) galaxies (see also Bhandari et al. 2018; Heintz et al. 2020).

Several hypotheses have been proposed for FRB progenitor systems (Platts et al. 2019), from eruptions on the surfaces of highly-magnetized neutron stars (i.e., magnetars; Popov & Postnov 2013; Lyubarsky 2014; Kulkarni et al. 2014; Katz 2016; Beloborodov 2017; Kumar et al. 2017; Metzger et al. 2017; Wadiasingh & Timokhin 2019; Beniamini et al. 2020) to accretion-induced collapse of neutron stars into black holes (Falcke & Rezzolla 2014). Notably, repeating FRBs exhibit pulse widths $> 4\sigma$ longer than those without multiple detected bursts (CHIME/FRB Collaboration et al. 2019), suggesting that there may be multiple progenitor channels. In addition, the recent detection of an FRB-like event from the Galactic magnetar SGR 1935+2154 suggests that at least a subset of repeating, extragalactic FRBs originate from magnetars (CHIME/FRB Collaboration et al. 2020a; Bochenek et al. 2020; Lu et al. 2020; Margalit et al. 2020a). This interpretation is complicated in part by evidence that FRB hosts lack a clear association to star formation (although some studies suggest FRBs can be produced via magnetars that do not trace star formation; see, e.g., Margalit et al. 2019; Safarzadeh et al. 2020; Bochenek et al. 2020).

Precise localization of FRBs has also enabled both targeted and untargeted follow up at wavelengths spanning from opti-

cal (Hardy et al. 2017; Bhandari et al. 2018; Andreoni et al. 2020) to X-ray (Petroff et al. 2015; Scholz et al. 2016; Pilia et al. 2020; Tavani et al. 2020; Scholz et al. 2020) to gamma-ray wavelengths (Yamasaki et al. 2016; Best & Bazo 2019; Cunningham et al. 2019; Guidorzi et al. 2019, 2020), primarily for the well-localized, repeating bursts FRB 121102 and FRB 180916. So far these searches have revealed no potential counterparts for extragalactic FRBs (e.g., Chen et al. 2020) apart from a 100 s duration gamma-ray transient detected at the 3.2σ level by the Neil Gehrels *Swift* Observatory (*Swift*; Gehrels et al. 2004) and contemporaneous with a burst from FRB 131104 (DeLaunay et al. 2016), although the association may not be secure (Shannon & Ravi 2017; Gao & Zhang 2017).

Theoretical models predict optical emission spanning faint luminosities of $< 10^{39}$ erg s $^{-1}$ within seconds of the burst via synchrotron emission in the circumburst medium of the progenitor (Metzger et al. 2019). However, the best limits from optical follow up observations have only ruled out counterparts to bursts down to relatively unconstraining luminosities of $\approx 10^{45}$ erg s $^{-1}$ (Hardy et al. 2017) within milliseconds of a burst or $\approx 5 \times 10^{42}$ erg s $^{-1}$ within minutes of a burst (Andreoni et al. 2020). Recent constraints on the periodic activity window of the repeating FRB 180916.J0158+65 (hereafter FRB 180916; CHIME/FRB Collaboration et al. 2020b) offer a unique opportunity to target emission from a FRB counterpart at non-radio wavelengths. In addition to untargeted optical observations from the Zwicky Transient Facility (Andreoni et al. 2020), Pilia et al. (2020) and Zampieri et al. (2020) reported high-speed optical observations with the 1.2m Galileo telescope during a burst that limit the Sloan *i*-band fluence of FRB 180916 to < 0.151 Jy ms. Additional multi-band follow up of this source will further benefit from the known 16.3 day period, suggesting that the counterpart is highly active on this timescale (CHIME/FRB Collaboration et al. 2020b). The relatively low redshift ($z = 0.0337$ with an implied luminosity distance of $D_L \approx 150$ Mpc; CHIME/FRB Collaboration et al. 2020b) means that any observations will yield significantly deeper constraints than those for FRBs previously targeted at optical wavelengths (e.g., FRB 121102; Hardy et al. 2017; Bhandari et al. 2018).

Here we discuss targeted optical follow up of FRB 180916 with the Apache Point Observatory (APO) 3.5m telescope. These observations were obtained contemporaneously with observations from the Canadian Hydrogen Intensity Mapping Experiment (CHIME) on 3 September 2020. During the observations, CHIME detected a radio burst at a location and dispersion measure consistent with previous bursts from FRB 180916 (CHIME/FRB Collaboration et al. 2020b; Marcote et al. 2020). At the time of the burst and for 30 minutes thereafter, we observed the FRB 180916 host galaxy with the APO telescope, but we did not detect any transient optical

emission at the FRB site. Based on the non-detections, we place constraints on the allowed burst properties and circumburst density in the synchrotron maser model. We discuss the timing and details of our observations in Section 2. In Section 3, we analyze these limits in the context of realistic optical counterparts to FRBs and discuss the implications of these limits for future follow up efforts. We summarize our findings in Section 4.

2. OBSERVATIONS

We targeted FRB 180916 on 3 September 2020 with the APO 3.5m telescope, mounted with the Astrophysical Research Consortium Telescope Imaging Camera (ARCTIC; Huehnerhoff et al. 2016). Our observations began (i.e., the camera shutter opened) at UTC 2020-09-03 11:05:39.7503. Each exposure sequence was a 3×30.33 s set of images in a single band (except for the third and fourth set of *g*-band exposures, which consisted of 2 and 4 exposures, respectively), following a $i \rightarrow r \rightarrow g$ pattern for 9 images per pattern or 36 images over the full set of observations (Table 1). The average time per exposure is 30.3 s over 2221.7 s for an observing efficiency of $\approx 49\%$. In addition, we obtained follow up observations on 13 September 2020 in *gri* bands with 3×100 s exposures to use as templates for comparison to the previous epoch. We show example *r* and *i*-band images obtained within 2 min from the topocentric radio burst arrival time in Figure 1.

The radio burst occurred during our first *gri* sequence when the second *r*-band image was exposing, implying that 32 out of 36 of our exposures occurred around or after the burst arrival time. Based on the topocentric burst time at 400 MHz provided by CHIME¹, the radio burst arrival time was 6.908 s after the shutter opened and 23.442 s before the shutter closed for this exposure. Thus including the second *r*-band exposure, approximately 32×30.33 s of cumulative exposure time was obtained during or immediately after the time of burst. The exact time the shutter opened and closed is given in Table 1 along with the relative time (in seconds) from the radio burst arrival.

The time of arrival for an FRB is frequency (ν) dependent following a ν^{-2} dispersion law (Tanenbaum et al. 1968). Variation in the burst arrival time is used to quantify the dispersion measure (DM) along the line of sight to the burst, a value that correlates with the column of electrons to the source and thus can be used to measure electron densities in the intergalactic medium (Petroff et al. 2016; Shannon et al. 2018; Macquart & Ekers 2018; Petroff et al. 2019b; Macquart et al. 2020). The DM for the FRB 180916 burst on 3 September 2020 was 352.6 ± 3.2 pc cm $^{-3}$, consistent with previ-

¹ 2020-09-03T11:10:32.495964Z;
180916.J0158+65

<https://www.chime-frb.ca/repeaters/>

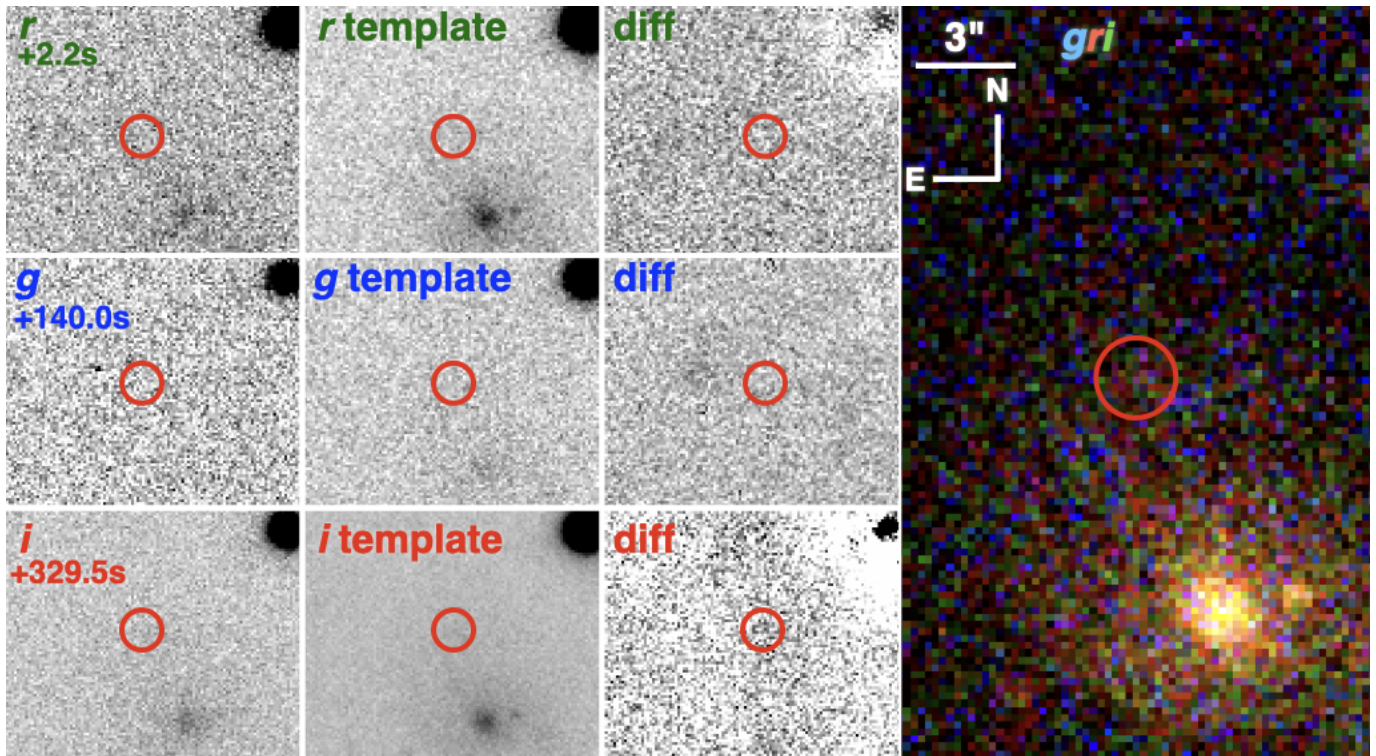


Figure 1. *Upper row:* r -band image starting from +2.2 s relative to the dispersion-corrected burst arrival time, our r -band template from 13 September 2020, and the difference between the two frames. There is no signature of transient emission at the FRB location (red circles). *Middle row:* Same as the top row for our g -band image starting at +140.0 s. *Bottom row:* Same as the top row for our i -band image starting at +329.5 s. *Right:* RGB (igr) image showing all of our stacked, post-burst data and centered on the location of the burst.

ous measurements toward the repeater (CHIME/FRB Collaboration et al. 2020b; Marcote et al. 2020). Based on this measurement, we can estimate the arrival time for the corresponding r -band optical emission from the FRB observed at 400 MHz, which would be earlier as it occurred at a higher frequency. Following equation (1) in Cordes & Chatterjee (2019) (see also Tanenbaum et al. 1968), we estimate that the burst arrival time in the optical was 9.1 s earlier than at 400 MHz, implying an arrival time of UTC 2020-09-03 11:10:23.4, which we use throughout this paper as the reference point for the “dispersion-corrected burst arrival time.”

We reduced all ARCTIC data using a custom-built pipeline based on the `photpipe` imaging and photometry package (Rest et al. 2005; Kilpatrick et al. 2018). Each frame was corrected for bias and flat-fielded using bias and sky flat field frames obtained in the same instrumental configuration. We registered the images using 2MASS astrometric standards (Skrutskie et al. 2006) observed in the field of each image. Finally, we performed point spread function (PSF) photometry using `DoPhot` (Schechter et al. 1993) and calibrated the gri data using PS1 DR2 standard stars in each image (Flewelling et al. 2016). We subtracted the observations taken on 13 September 2020 from all 3 September 2020 observations using `HOTPANTS` (Becker 2015) to perform PSF convolution and difference imaging and then estimated the

3σ limiting magnitude at the position of FRB 180916 (from Marcote et al. 2020) with fake star injection. Thus the limits we derive can be interpreted as the maximum average in-band specific flux integrated over the 30.33 s window for each exposure or the entire observation window for the limits in the stacked data. As shown in Table 1, the typical limiting magnitude of each individual frame was ≈ 24.5 mag in gri bands or ≈ 26.0 mag in the stacked frames.

3. CONSTRAINING THE FRB EMISSION MECHANISM

The timeline for our exposures immediately after the radio burst is shown in Figure 2. We estimate based on the 9.1 s dispersive delay of the radio emission that the FRB occurred approximately 2.2 s before the shutter opened for our second r -band exposure. Thus our closest and most constraining image of FRB 180916 covered roughly 2.2 to 30.5 seconds relative to the burst arrival time. Our full, post-burst data set covers approximately +2.2 s to +1938.1 s relative to the dispersion-corrected burst arrival time in gri (Table 1). We also give the limiting magnitudes for times before the expected burst arrival time, but in the context of the models below, we do not consider these data as no optical emission is predicted.

We give the 3σ limiting magnitude in AB magnitudes both for a source at the location of FRB 180916 in each image and

in absolute magnitudes after correcting for the distance modulus and Milky Way foreground extinction $A_V = 2.767$ mag (from [Schlafly & Finkbeiner 2011](#)). We assume the redshift $z = 0.0337 \pm 0.0002$ derived for the host galaxy of FRB 180916 in [Marcote et al. \(2020\)](#) along with [Planck Collaboration et al. \(2016\)](#) cosmology, from which we derive a luminosity distance of $D_L = 153 \pm 1$ Mpc or a distance modulus of $\mu = 35.92 \pm 0.02$ mag.

We compare these limits to predictions of the synchrotron maser model as shown in [Metzger et al. \(2019\)](#); [Margalit et al. \(2020b\)](#) (but also see [Lyubarsky 2014](#); [Beloborodov 2017, 2020](#), for slightly different optical predictions, especially at times comparable to the burst duration when the total luminosity may be larger). In the [Metzger et al. \(2019\)](#) formalism for this model, the radio burst originates in a shock from a radially-expanding plasmoid launched from a central engine (e.g., a magnetar). The relativistic plasmoid may be decelerated by surrounding material in the immediate environment of the engine. If this material is sufficiently magnetized, synchrotron maser emission will be produced ([Plotnikov & Sironi 2019](#)). In the model of [Metzger et al. \(2019\)](#); [Margalit et al. \(2020b\)](#) (and first proposed by [Beloborodov 2017](#)) the surrounding upstream material is baryon-loaded ejecta expelled in previous flaring activity of the magnetar.

One prediction of this model (see Section 4 in [Metzger et al. 2019](#)) is that there should be a broadband (incoherent) synchrotron afterglow that will accompany and follow the FRB. On timescales similar to the FRB duration, this afterglow will peak in hard X-rays/gamma-rays, but it can subsequently cascade through optical bands on timescales of minutes post-burst. Assuming a plasmoid ejection event with energy E_{flare} that lasts for a duration δt , and a fractional magnetization σ in the material upstream from the forward shock, the peak frequency ν_{syn} of this synchrotron afterglow will vary with time t from the burst event approximately as (following equations (56)-(57) in [Metzger et al. 2019](#))

$$h\nu_{\text{syn}}(t_{\text{dec}}) = 57 \text{ MeV} \left(\frac{\sigma}{0.1}\right)^{1/2} \left(\frac{E}{10^{43} \text{ erg}}\right)^{1/2} \left(\frac{\delta t}{10^{-3} \text{ s}}\right)^{-3/2} \quad (1)$$

$$h\nu_{\text{syn}} = \begin{cases} h\nu_{\text{syn}}(t_{\text{dec}}) \left(\frac{t}{t_{\text{dec}}}\right)^{-1}, & t < t_{\text{dec}} \\ h\nu_{\text{syn}}(t_{\text{dec}}) \left(\frac{t}{t_{\text{dec}}}\right)^{-3/2}, & t > t_{\text{dec}} \end{cases} \quad (2)$$

where $t_{\text{dec}} \approx \delta t \approx 10^{-4}$ s, which is a fiducial parameter and can be set to the observed duration of the burst. The peak synchrotron frequency cascades down to the synchrotron cooling frequency (ν_c), which depends on properties of the circumburst material. Motivated by constraints on the engine of FRB121102 ([Margalit & Metzger 2018](#)), [Metzger et al. \(2019\)](#) considered previously ejected baryonic-shells as the circumburst material, and parameterized ν_c in terms of the velocity of the ejected material ($\beta = v/c$), the

average rate at which this material is injected into the surrounding medium (\dot{M}), and the characteristic time between ejection events (ΔT). Following equation (60) in [Metzger et al. \(2019\)](#), the cooling frequency is

$$h\nu_c = 9 \text{ keV} \left(\frac{\sigma}{0.1}\right)^{-3/2} \left(\frac{\beta}{0.5}\right)^3 \left(\frac{\dot{M}}{10^{21} \text{ g s}^{-1}}\right)^{-1} \left(\frac{t}{10^{-3} \text{ s}}\right)^{-1/2} \left(\frac{\Delta T}{10^5 \text{ s}}\right)^2. \quad (3)$$

Critically, the average period ΔT between bursts, although directly observable and constrained for FRB 180916 as 16.3 days ([CHIME/FRB Collaboration et al. 2020b](#)), simply depends on the circumburst density under the assumption that the surrounding medium is filled by ions from previous mass ejection events. In [Equation 3](#), we assume that this medium is characterized by a series of discrete ion shells with a number density of ions in the surrounding medium $n_{\text{ext}} \propto (\Delta T)^{-2}$ where the density profile with radius r from the source of the burst is $n_{\text{ext}} \propto r^{-k}$. For the discrete shells case, we adopt a $k = 0$ following the prescription in [Margalit et al. \(2020b\)](#).

We find that this circumburst density profile provides a natural model for the environment of a source with episodic ejections, but this profile need not be the case if the FRB progenitor erupts inside of a steady wind ($k = 2$), a low-density, ambient medium, or homologously expanding shells of ejecta from a supernova. These density profiles would imply significantly different optical evolution than predicted here, which in general is less constraining as the circumburst density at the radius of the shock drops significantly on timescales much longer than the burst duration. In addition, although the radio burst itself would probe the density of the circumburst medium out to a radius $r_{\text{dec}} \approx 2\Gamma^2 ct_{\text{dec}}$ ($\approx 10^{12}\text{--}10^{13}$ cm for $t_{\text{dec}} = 10^{-3}$ s and a Lorentz factor Γ ; [Metzger et al. 2019](#); [Margalit et al. 2020b](#)), we assume that this density profile continues outward for several decades in distance because most of the optical emission is produced at time $t_{\text{syn}} \gg t_{\text{dec}}$ when the FRB is emitted (see [Equation 7](#) below). This assumption may hold true if the medium is filled via the continuous ejection of material from a magnetar, but it is a caveat to the following analysis.

Throughout the rest of this paper, we transform ΔT in (i.e., in [Equation 3](#)) to n_{ext} , representing the circumburst density at a radius from the progenitor $r_{\text{dec}} = 2\Gamma^2 ct_{\text{dec}}$, following equation (32) in [Metzger et al. \(2019\)](#) such that

$$h\nu_c = 2.3 \text{ keV} \left(\frac{\sigma}{0.1}\right)^{-3/2} \left(\frac{n_{\text{ext}}}{10^3 \text{ cm}^{-3}}\right)^{-1} \left(\frac{t}{10^{-3} \text{ s}}\right)^{-1/2}. \quad (4)$$

The optical light curve is luminous until after the time when the peak synchrotron frequency is equal to the cooling frequency, at which point cooling is no longer efficient. Although the light curve will briefly continue to rise at $t^{1/2}$ in this regime, as ν_{syn} drops below the observing frequency ($\approx 3.6\text{--}7.5 \times 10^{14}$ Hz for gri) the optical luminosity will decline exponentially. We include this cutoff in our light curves by rescaling the optical luminosity by $\exp(-(\nu/\nu_{\text{syn}} - 1))$ when $\nu > \nu_{\text{syn}}$. Overall, we use equations (63)-(64) in Metzger et al. (2019) to model the peak luminosity (L_{pk}) and specific luminosity (L_ν) of the optical light curve at $t > t_{\text{dec}}$ as

$$L_{\text{pk}} = 10^{45} \text{ erg s}^{-1} \left(\frac{E_{\text{flare}}}{10^{43} \text{ erg}} \right) \left(\frac{t}{10^{-3} \text{ s}} \right)^{-1} \quad (5)$$

$$\nu L_\nu = \begin{cases} L_{\text{pk}} \left(\frac{\nu}{\nu_c} \right)^{4/3} \left(\frac{\nu_c}{\nu_{\text{syn}}} \right)^{1/2}, & \nu < \nu_c \\ L_{\text{pk}} \left(\frac{\nu}{\nu_{\text{syn}}} \right)^{1/2}, & \nu_c < \nu < \nu_{\text{syn}}. \end{cases} \quad (6)$$

We note that in Figure 2 the light curve begins to decline when $\nu = \nu_{\text{syn}}$, which occurs at

$$t_{\text{syn}} = 82.6 \text{ s} \left(\frac{\lambda}{5000 \text{ \AA}} \right)^{2/3} \left(\frac{\sigma}{0.1} \right)^{1/3} \left(\frac{E_{\text{flare}}}{10^{43} \text{ erg}} \right)^{1/3} \quad (7)$$

where λ is the observed wavelength. Thus for r -band ($\approx 6231 \text{ \AA}$), the timescale for $E_{\text{flare}} = 10^{45} \text{ erg}$ and $\sigma = 0.3$ (as in Metzger et al. 2019) is $\approx 640 \text{ s}$, or about 1/3 of our observation window. This is also significantly longer than any individual observation, implying that our limits for the full set or some subset of our observations are much more constraining than limits from individual exposures.

Moreover, the predicted luminosity is comparable to or brighter than our limits in the 10^{45} erg case, with the peak occurring around this time at $\nu L_\nu = 8 \times 10^{40} \text{ erg s}^{-1}$. We also note that higher densities will result in significantly more luminous bursts with $\nu L_\nu \propto n_{\text{ext}}^{5/6}$ as we are always in the regime where the optical frequency is below the cooling frequency.

Assuming the synchrotron maser model with the same fiducial parameters given above, we consider varying the energy scale of the burst $\log(E_{\text{flare}}/\text{erg}) \in [41.2, 47.4]$ and circumburst ion density $\log(n_{\text{ext}}/\text{cm}^{-3}) \in [1, 6.2]$. We then model the total in-band emission for our gri observations by calculating the average specific luminosity integrated over the time of each observation relative to the burst arrival time and averaged over frequencies corresponding to the filter response function. We convert this value to a predicted apparent magnitude assuming the distance modulus and foreground extinction given above. For each model in our grid, if the computed apparent magnitude is brighter than any of

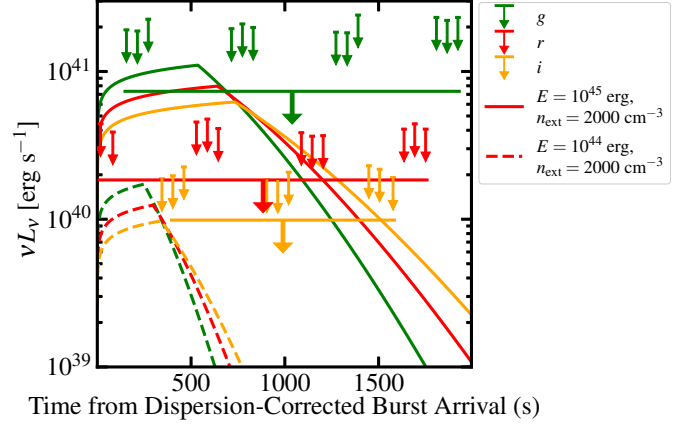


Figure 2. Optical light curves of the synchrotron afterglow from a magnetar-driven burst as described in Section 3. We compare the predicted specific luminosity in νL_ν for r band and two sets of model light curves corresponding to injected energies $E = 10^{45} \text{ erg}$ (solid lines) and $E = 10^{44} \text{ erg}$ (dashed lines) in g (green), r (red), and i (orange) to the limits derived from our optical data. Otherwise, the models assume our fiducial parameters as given in Section 3 (see also figure 8 in Metzger et al. 2019) and the median circumburst density ($n_{\text{ext}} \approx 2000 \text{ cm}^{-3}$) in Margalit et al. (2020b). The model is predicted to decline rapidly at the time t_{syn} where the peak of the synchrotron spectrum cascades below the observing frequency.

our 3σ limiting magnitudes given in Table 1 (including the 3σ limits for the stacked, post-burst imaging), we consider that model ruled out as shown through the greyed-out region from Figure 3.

This model assumes that both the circumburst and interstellar host extinction are negligible in the context of likely optical counterparts. In an ion-rich medium the optical depth would be dominated by electron scattering with $\tau \approx 10^{-7}$ following equation (33) in Metzger et al. (2019).

The interstellar burst host extinction could be dominated by dust with no indication in the radio signal, and indeed, FRB 180916 appears coincident with a small enhancement in the optical emission from its host galaxy (Marcote et al. 2020; Tendulkar et al. 2020). This finding suggests that FRB 180916 is located within or near a star-forming region (it is 250 pc from a young stellar clump based on a $\text{H}\alpha$ detection in *Hubble Space Telescope* imaging; Tendulkar et al. 2020) where there could be excess gas and dust obscuring the optical counterpart (similar to, e.g., stripped-envelope SNe, which evolve from very massive, young stars and thus are observed with high average interstellar host extinction near their birth environments; Stritzinger et al. 2018).

A constraint on the total extinction in the FRB 180916 host galaxy comes from the DM observed toward this source, which is known to be on average $\approx 350 \text{ pc cm}^{-3}$ and $352.6 \pm 3.2 \text{ pc cm}^{-3}$ for the 3 September 2020 burst. From this value, we account for Milky Way interstellar disper-

sion adopting 171.7 pc cm^{-3} on the line-of-sight toward FRB 180916 (using the NE2001 model of Cordes & Lazio 2002) as well as 50 pc cm^{-3} for the Milky Way halo, although this latter value ranges from 30–80 pc cm^{-3} (e.g. Prochaska & Zheng 2019; Platts et al. 2020). To account for the intergalactic DM, we adopt the relation in Macquart et al. (2020) at $z = 0.0337$, which gives $56 \pm 20 \text{ pc cm}^{-3}$. Multiplying the residual DM by $1 + z$, we obtain a source-frame DM host-galaxy contribution in the line-of-sight to FRB 180916 of $75 \pm 30 \text{ pc cm}^{-3}$. This is equivalent to a hydrogen column density of $N_H = 2.3 \pm 1.5 \times 10^{21} \text{ cm}^{-2}$ following the locally-derived relation in He et al. (2013). Finally, this column yields $A_V \approx 1.0 \pm 0.6 \text{ mag}$ following Güver & Özel (2009), but we acknowledge a significant systematic uncertainty on this value. Fitting the dust content in the FRB 180916 host yields a much lower dust content of $E(B - V) = 0.12 \text{ mag}$ (Heintz et al. 2020), which implies $A_V = 0.4 \text{ mag}$ assuming $R_V = 3.1$. Although this value is not a line-of-sight probe similar to the DM, it is nominally consistent with the lower bound of our interstellar host extinction estimate. Therefore, we conservatively adopt $A_V = 0.50 \text{ mag}$ with $R_V = 3.1$ to model our observations below and assume a Cardelli et al. (1989) reddening relation, implying that $A_g = 0.53 \text{ mag}$, $A_r = 0.37 \text{ mag}$, and $A_i = 0.27 \text{ mag}$ due to interstellar dust in the host of FRB 180916.

To place our final limiting magnitudes in context, we consider the full range of circumburst densities corresponding to FRB 180916 in Margalit et al. (2020b). In general, the energy of the burst E_{flare} can be estimated from the equivalent isotropic energy in a single radio burst (E_{radio}) following Margalit et al. (2020a,b) as

$$\frac{E_{\text{radio}}}{E_{\text{flare}}} \approx 8.6 \times 10^{-3} f_e f_\xi \left(\frac{\nu_{\text{obs}} t_{\text{FRB}}}{1 \text{ GHz ms}} \right)^{-1/5} \quad (8)$$

where the observation frequency ν_{obs} and the total burst duration t_{FRB} are known from radio observations, the ratio of electron to ion number densities in the upstream medium $f_e = 0.5$ is assumed, and the synchrotron maser efficiency is $f_\xi \approx 10^{-3}$ (Plotnikov & Sironi 2019). We do not currently know the fluence (S_ν) or duration of the 3 September 2020 radio burst from FRB 180916, and so we assume that it followed the distribution from CHIME/FRB Collaboration et al. (2020b), with $E_{\text{radio}} = 4\pi D^2 \nu S_\nu$ at 400 MHz of $(1.1\text{--}39.8) \times 10^{37} \text{ erg}$ and t_{FRB} of $\approx 0.6\text{--}8.6 \text{ ms}$ (corresponding to $E_{\text{flare}} = 0.04\text{--}1.45 \times 10^{43} \text{ erg}$). Assuming an average $E_{\text{radio}} = 6.8 \times 10^{37} \text{ erg}$ and $t_{\text{FRB}} = 3.7 \text{ ms}$ for bursts with well-measured fluence and duration in CHIME/FRB Collaboration et al. (2020b), we estimate that the average energy per burst is $E_{\text{flare}} = 2.5 \times 10^{42} \text{ erg}$ for FRB 180916 as shown in Figure 3.

This places the average optical counterpart well outside the range of detectability for our observations and the model parameters above (noting the greyed-out region in Figure 3 and assuming FRB 180916 parameters -red error bars- from Margalit et al. 2020b). From the expected moment of dispersion-corrected burst arrival at optical wavelengths, the timescale for an optical light curve with $E_{\text{flare}} = 2.5 \times 10^{42} \text{ erg}$ and $\sigma = 0.3$ is $t_{\text{syn}} \approx 87 \text{ s}$, implying that most of our imaging after this point is not very constraining in the context of likely optical counterparts.

Moreover, for a circumburst density $n_{\text{ext}} = 2000 \text{ cm}^{-3}$ (roughly the median value for FRB 180916 in Margalit et al. 2020b), the burst would have an optical luminosity $\nu L_\nu \approx 6 \times 10^{38} \text{ erg s}^{-1}$ ($M \approx -8 \text{ mag}$ or $m \approx 28 \text{ mag}$ at 150 Mpc) on the timescale t_{syn} . This is below the threshold of detectability for nearly all optical telescopes, even assuming infinite integration time. For high-speed optical imagers that can observe on the timescale of tens of ms around a burst (e.g., the 2.4m Thai National Telescope/ULTRASPEC with $m_{\text{limit}} \approx 16.8 \text{ mag}$ over 70 ms; Hardy et al. 2017), the detection threshold is shallower by several orders of magnitude. Thus to detect a burst at optical wavelengths with a light curve similar to those above, a large aperture telescope and an anomalously energetic burst with $E_{\text{flare}} > 10^{44} \text{ erg}$ would be needed (following our limits and the maximum densities inferred for FRB 180916 in Figure 3).

On the other hand, if the source were in a highly active state with significantly larger energies and shorter timescale between bursts, this might boost the circumburst density and the corresponding optical signal and potentially place the counterpart within the range of detectability. The shortest timescales between bursts for FRB 180916 are only 0.5 milliseconds (observed on 19 Dec 2019; CHIME/FRB Collaboration et al. 2020b), or $\approx 100 \text{ s}$ in cases where $\Delta T/t_{\text{FRB}} \gg 1$. Taking $\Delta T = 100\text{--}1.4 \times 10^6 \text{ s}$ as the full range of burst periods and assuming an extremely energetic burst with $E_{\text{flare}} = 10^{44} \text{ erg}$, the circumburst density might exceed 10^4 cm^{-3} (as with FRB 121102, the burst with the highest inferred circumburst density in Margalit et al. 2020b). Based on the assumed $n_{\text{ext}} \propto \Delta T^{-2}$ and $L_{\text{pk}} \propto n_{\text{ext}}^{5/6}$ scaling above, this would require a change in average period of at least a factor of 5 or $\Delta T \approx 3.3 \text{ days}$.

The FRB may have outbursts on timescales significantly shorter than 3.3 days (CHIME/FRB Collaboration et al. 2020b), although it is unclear whether these bursts would have similar flare energies or lead to a significantly denser circumburst medium in the magnetar-driven synchrotron maser model we adopt above. Moreover, the $k = 0$ density profile discussed above may not be representative at all projected radii if the burst properties change significantly with time.

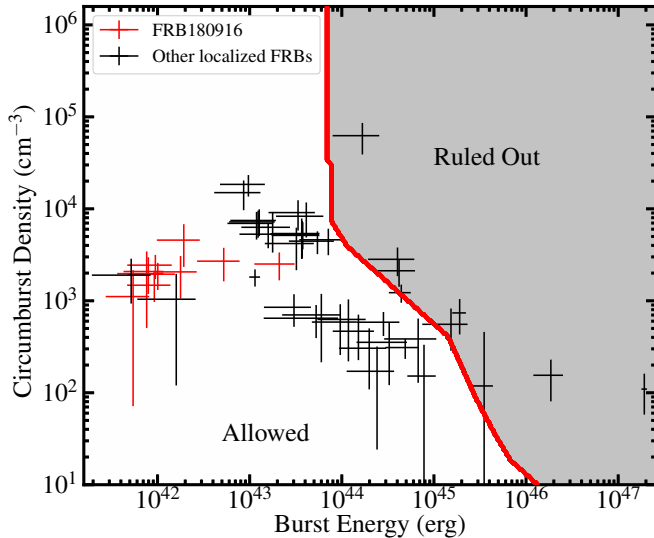


Figure 3. Flare energy (E_{flare}) and circumburst density (n_{ext}) parameter space for FRBs for Metzger et al. (2019) synchrotron maser light curves as described in Section 3. We show the range inferred for individual bursts as error bars (from Margalit et al. 2020a) and FRB 180916 bursts shown in red. We demonstrate the energy-density parameter range that we can rule out for the 3 September 2020 burst of FRB 180916 and using our optical limits as a grey region.

Thus while it is unclear if FRB 180916 can briefly enter the parameter range we rule out in Figure 3, we would only require moderately deeper imaging or more frequent and energetic bursts to detect the optical counterpart. Finally, detailed analysis of the 3 September 2020 radio burst detected by CHIME will provide a direct constraint on the circumburst density (following equation (8) in Margalit et al. 2020b).

For future optical follow up efforts, this implies that in the context of the baryonic-shell version of the synchrotron maser model, the most promising search strategies will be to target FRB 180916 with a 8–10 m telescopes when it is in an active state and likely to have one or more bursts. On the other hand, if the burst profile is significantly more luminous on short timescales after the burst (e.g., following the models of Beloborodov 2020), high-speed cameras such as ULTRASPEC (Hardy et al. 2017) on large aperture telescopes will yield the strongest constraints on potential optical counterparts. Moreover, if the burst period decreases and the circumburst density is temporarily enhanced, the optical counterpart may be bright such that prompt and/or long-lived counterparts are detectable.

4. CONCLUSIONS

REFERENCES

Ai, S., Gao, H., & Zhang, B. 2020, arXiv e-prints, arXiv:2007.02400

We presented APO 3.5m/ARCTIC observations of FRB 180916 around the time of a fast radio burst. Comparing to models of synchrotron maser emission corresponding to the broadband, relatively long-lived counterpart to a radio burst, we find:

1. Our observations are constraining for synchrotron maser emission in cases where the energy per burst is larger than $\approx 10^{44}$ erg and the circumburst density is greater than 10^4 cm^{-3} .
2. Comparing to previous constraints on the FRB 180916 burst energy from Margalit et al. (2020a), our limits are not constraining for the predicted burst parameters. However, if the circumburst density is temporarily enhanced when the FRB progenitor is highly active and multiple discrete bursts occur (e.g., on 19 Dec 2019 and 4 Feb 2020; CHIME/FRB Collaboration et al. 2020b), the predicted optical light curve could exceed the magnitude limit achievable by large aperture telescopes.
3. Future optical follow up efforts that target emission similar to the synchrotron maser model will benefit from joint optical and radio observations of FRB 180916 longer than 30 min and during its active phase when multiple bursts are likely to occur.

ACKNOWLEDGMENTS

We thank J. X. Prochaska for helpful comments on this manuscript. C.D.K. acknowledges support through a NASA grant in support of *Hubble Space Telescope* program AR-16136. K.E.H. acknowledges support by a Project Grant (162948–051) from The Icelandic Research Fund. W.F. acknowledges support by the National Science Foundation under grant Nos. AST-1814782 and AST-1909358. B.M. is supported by NASA through the NASA Hubble Fellowship grant #HST-HF2-51412.001-A awarded by the Space Telescope Science Institute, which is operated by the Association of Universities for Research in Astronomy, Inc., for NASA, under contract NAS5-26555. Based on observations obtained with the Apache Point Observatory 3.5-meter telescope, which is owned and operated by the Astrophysical Research Consortium.

Facilities: APO 3.5m (ARCTIC)

Andreoni, I., Lu, W., Smith, R. M., et al. 2020, ApJL, 896, L2

Table 1. APO 3.5m/ARCTIC Observations of FRB 180916

Shutter Open (Epoch) ^a	Shutter Closed (Epoch) ^a	Cumulative Exposure	Filter	α^b	δ^b	m_{lim}^c	M_{lim}^d
(s)	(s)	(s)		(J2000)	(J2000)	(AB mag)	(AB mag)
11:05:39.7503Z (-283.6)	11:06:10.0854Z (-253.3)	30.335	<i>i</i>	01:57:58.831	+65:43:05.13	24.87	-12.77
11:07:05.7701Z (-197.6)	11:07:36.1048Z (-167.3)	30.335	<i>i</i>	01:57:57.938	+65:43:05.02	24.75	-12.88
11:08:20.3947Z (-123.0)	11:08:50.7298Z (-92.7)	30.335	<i>i</i>	01:57:57.972	+65:43:00.04	24.82	-12.81
11:09:27.4379Z (-56.0)	11:09:57.7672Z (-25.6)	30.329	<i>r</i>	01:57:58.777	+65:43:05.05	24.86	-13.36
11:10:25.5880Z (2.2)	11:10:55.9377Z (32.5)	30.350	<i>r</i>	01:57:57.966	+65:43:05.14	24.87	-13.35
11:11:31.1064Z (67.7)	11:12:01.4421Z (98.0)	30.336	<i>r</i>	01:57:57.937	+65:42:59.95	25.02	-13.21
11:12:43.4415Z (140.0)	11:13:13.7769Z (170.4)	30.335	<i>g</i>	01:57:58.739	+65:43:05.26	24.60	-14.65
11:13:41.9013Z (198.5)	11:14:12.2416Z (228.8)	30.340	<i>g</i>	01:57:57.941	+65:43:05.20	24.62	-14.63
11:14:39.9834Z (256.6)	11:15:10.3232Z (286.9)	30.340	<i>g</i>	01:57:57.935	+65:43:00.17	24.42	-14.83
11:15:52.9075Z (329.5)	11:16:23.2385Z (359.8)	30.331	<i>i</i>	01:57:58.825	+65:43:04.73	25.00	-12.64
11:16:51.1111Z (387.7)	11:17:21.4439Z (418.0)	30.333	<i>i</i>	01:57:57.990	+65:43:04.33	24.94	-12.69
11:17:50.0614Z (446.7)	11:18:20.4010Z (477.0)	30.340	<i>i</i>	01:57:57.972	+65:42:59.66	24.79	-12.84
11:18:56.7009Z (513.3)	11:19:27.0366Z (543.6)	30.336	<i>r</i>	01:57:58.771	+65:43:04.94	24.85	-13.38
11:19:55.0051Z (571.6)	11:20:25.3396Z (601.9)	30.334	<i>r</i>	01:57:57.993	+65:43:05.02	24.80	-13.43
11:20:53.2300Z (629.8)	11:21:23.5680Z (660.2)	30.338	<i>r</i>	01:57:57.947	+65:42:59.99	24.96	-13.27
11:22:03.6474Z (700.2)	11:22:33.9856Z (730.6)	30.338	<i>g</i>	01:57:58.721	+65:43:05.29	24.58	-14.67
11:23:01.7765Z (758.4)	11:23:32.1159Z (788.7)	30.339	<i>g</i>	01:57:57.961	+65:43:05.07	24.51	-14.75
11:23:59.3999Z (816.0)	11:24:29.7394Z (846.3)	30.337	<i>g</i>	01:57:57.981	+65:43:00.28	24.56	-14.69
11:25:12.1161Z (888.7)	11:25:42.4525Z (919.1)	30.336	<i>i</i>	01:57:58.801	+65:43:04.87	25.02	-12.62
11:26:10.6413Z (947.2)	11:26:40.9768Z (977.6)	30.335	<i>i</i>	01:57:57.963	+65:43:04.80	25.02	-12.61
11:27:08.5896Z (1005.2)	11:27:38.8951Z (1035.5)	30.306	<i>i</i>	01:57:57.980	+65:42:59.81	24.89	-12.75
11:28:16.3330Z (1072.9)	11:28:46.6618Z (1103.3)	30.329	<i>r</i>	01:57:58.774	+65:43:04.93	25.03	-13.20
11:29:13.7910Z (1130.4)	11:29:44.1262Z (1160.7)	30.335	<i>r</i>	01:57:57.969	+65:43:04.86	25.09	-13.14
11:30:12.4674Z (1189.1)	11:30:42.8033Z (1219.4)	30.336	<i>r</i>	01:57:57.988	+65:43:00.04	25.08	-13.15
11:31:20.9344Z (1257.5)	11:31:51.2694Z (1287.9)	30.335	<i>g</i>	01:57:58.758	+65:43:05.19	24.64	-14.61
11:32:20.6130Z (1317.2)	11:32:50.9150Z (1347.5)	30.302	<i>g</i>	01:57:57.943	+65:43:05.17	24.65	-14.60
11:33:18.7291Z (1375.3)	11:33:49.0651Z (1405.7)	30.336	<i>i</i>	01:57:57.969	+65:43:00.09	22.73	-14.90
11:34:16.2548Z (1432.9)	11:34:46.5853Z (1463.2)	30.331	<i>i</i>	01:57:58.808	+65:43:04.75	24.77	-12.86
11:35:13.6288Z (1490.2)	11:35:43.9768Z (1520.6)	30.348	<i>i</i>	01:57:57.987	+65:43:04.90	24.83	-12.80
11:36:25.2157Z (1561.8)	11:36:55.5512Z (1592.2)	30.335	<i>r</i>	01:57:57.957	+65:42:59.96	25.57	-12.66
11:37:23.8992Z (1620.5)	11:37:54.1358Z (1650.7)	30.237	<i>r</i>	01:57:58.743	+65:43:05.36	24.97	-13.26
11:38:21.0860Z (1677.7)	11:38:51.4219Z (1708.0)	30.336	<i>r</i>	01:57:57.974	+65:43:04.88	24.88	-13.35
11:39:19.1340Z (1735.7)	11:39:49.4752Z (1766.1)	30.341	<i>g</i>	01:57:58.003	+65:43:00.10	25.99	-13.26
11:40:16.5898Z (1793.2)	11:40:46.9242Z (1823.5)	30.334	<i>g</i>	01:57:58.753	+65:43:05.38	24.40	-14.86
11:41:13.7692Z (1850.4)	11:41:44.1046Z (1880.7)	30.335	<i>g</i>	01:57:57.950	+65:43:05.31	24.45	-14.81
11:42:11.2244Z (1907.8)	11:42:41.5377Z (1938.1)	30.313	<i>g</i>	01:57:57.934	+65:43:05.21	24.39	-14.86
11:10:25.5880Z (2.2)	11:38:51.4219Z (1708.0)	364.10 ^e	<i>r</i>	01:57:57.877	+65:43:05.08	25.83	-12.40
11:12:43.4415Z (140.0)	11:42:41.5377Z (1938.1)	364.10 ^e	<i>g</i>	01:57:57.877	+65:43:05.08	25.84	-13.41
11:15:52.9075Z (329.5)	11:35:43.9768Z (1520.6)	273.08 ^e	<i>i</i>	01:57:57.877	+65:43:05.08	25.70	-11.94

^a All times are UTC on 2020-09-03. The relative epoch is given in seconds compared with the dispersion-corrected burst arrival time (UTC 2020-09-03 11:10:23.4) as described in Section 2.

^b Pointing center of our ARCTIC observation. Note that ARCTIC is a 2048×2048 imager with $\approx 0.232''$ pixels, for a $7.92' \times 7.92'$ field of view.

^c 3σ apparent limiting magnitude at the location of FRB 180916 averaged over the entire exposure.

^d 3σ absolute limiting magnitude accounting for a distance modulus $\mu = 35.92$ mag (Section 3) and foreground extinction from Schlafly & Finkbeiner (2011). The values in this table assume no interstellar host extinction, but we adopt $A_g = 0.53$ mag, $A_r = 0.37$ mag, and $A_i = 0.27$ mag following the discussion in Section 3.

^e Stacked exposure for all imaging after the expected optical arrival time of the 3 September 2020 burst for FRB 180916. The limiting magnitude is 3σ calculated empirically in the stacked frame as described in Section 3.

Bannister, K. W., Deller, A. T., Phillips, C., et al. 2019, *Science*, 365, 565

Becker, A. 2015, HOTPANTS: High Order Transform of PSF AND Template Subtraction, ascl:1504.004

Beloborodov, A. M. 2017, *ApJL*, 843, L26

—. 2020, *ApJ*, 896, 142

Beniamini, P., Wadiasingh, Z., & Metzger, B. D. 2020, *MNRAS*, 496, 3390

Best, S., & Bazo, J. 2019, *JCAP*, 2019, 004

- Bhandari, S., Keane, E. F., Barr, E. D., et al. 2018, *MNRAS*, 475, 1427
- Bochenek, C. D., Ravi, V., & Dong, D. 2020, arXiv e-prints, arXiv:2009.13030
- Caleb, M., Stappers, B. W., Rajwade, K., & Flynn, C. 2019, *MNRAS*, 484, 5500
- Cardelli, J. A., Clayton, G. C., & Mathis, J. S. 1989, *ApJ*, 345, 245
- Chatterjee, S., Law, C. J., Wharton, R. S., et al. 2017, *Nature*, 541, 58
- Chen, G., Ravi, V., & Lu, W. 2020, *ApJ*, 897, 146
- CHIME/FRB Collaboration, Andersen, B. C., Bandura, K., et al. 2019, *ApJL*, 885, L24
- CHIME/FRB Collaboration, Andersen, B. C., Bandura, K. M., et al. 2020a, arXiv:2005.10324, arXiv:2005.10324
- CHIME/FRB Collaboration, Amiri, M., Andersen, B. C., et al. 2020b, *Nature*, 582, 351
- Cordes, J. M., & Chatterjee, S. 2019, *ARA&A*, 57, 417
- Cordes, J. M., & Lazio, T. J. W. 2002, arXiv e-prints, astro
- Cunningham, V., Cenko, S. B., Burns, E., et al. 2019, *ApJ*, 879, 40
- DeLaunay, J. J., Fox, D. B., Murase, K., et al. 2016, *ApJL*, 832, L1
- Falcke, H., & Rezzolla, L. 2014, *A&A*, 562, A137
- Flewelling, H. A., Magnier, E. A., Chambers, K. C., et al. 2016, arXiv e-prints, arXiv:1612.05243
- Gao, H., & Zhang, B. 2017, *ApJL*, 835, L21
- Gehrels, N., Chincarini, G., Giommi, P., et al. 2004, *ApJ*, 611, 1005
- Guidorzi, C., Marongiu, M., Martone, R., et al. 2019, *ApJ*, 882, 100
- . 2020, *A&A*, 637, A69
- Güver, T., & Özel, F. 2009, *MNRAS*, 400, 2050
- Hardy, L. K., Dhillon, V. S., Spitler, L. G., et al. 2017, *MNRAS*, 472, 2800
- Hashimoto, T., Goto, T., On, A. Y. L., et al. 2020, *MNRAS*, 497, 4107
- He, C., Ng, C. Y., & Kaspi, V. M. 2013, *ApJ*, 768, 64
- Heintz, K. E., Prochaska, J. X., Simha, S., et al. 2020, arXiv e-prints, arXiv:2009.10747
- Huehnerhoff, J., Ketzbeck, W., Bradley, A., et al. 2016, in *Society of Photo-Optical Instrumentation Engineers (SPIE) Conference Series*, Vol. 9908, *Ground-based and Airborne Instrumentation for Astronomy VI*, 99085H
- Katz, J. I. 2016, *ApJ*, 826, 226
- Kilpatrick, C. D., Foley, R. J., Drout, M. R., et al. 2018, *MNRAS*, 473, 4805
- Kulkarni, S. R., Ofek, E. O., Neill, J. D., Zheng, Z., & Juric, M. 2014, *ApJ*, 797, 70
- Kumar, P., Lu, W., & Bhattacharya, M. 2017, *MNRAS*, 468, 2726
- Kumar, P., Shannon, R. M., Flynn, C., et al. 2020, *MNRAS*, arXiv:2009.01214
- Li, Y., & Zhang, B. 2020, *ApJL*, 899, L6
- Lorimer, D. R., Bailes, M., McLaughlin, M. A., Narkevic, D. J., & Crawford, F. 2007, *Science*, 318, 777
- Lu, W., Kumar, P., & Zhang, B. 2020, *MNRAS*, 498, 1397
- Lyubarsky, Y. 2014, *MNRAS*, 442, L9
- Macquart, J. P., & Ekers, R. 2018, *MNRAS*, 480, 4211
- Macquart, J. P., Prochaska, J. X., McQuinn, M., et al. 2020, *Nature*, 581, 391
- Marcote, B., Nimmo, K., Hessels, J. W. T., et al. 2020, *Nature*, 577, 190
- Margalit, B., Beniamini, P., Sridhar, N., & Metzger, B. D. 2020a, *ApJL*, 899, L27
- Margalit, B., Berger, E., & Metzger, B. D. 2019, *ApJ*, 886, 110
- Margalit, B., & Metzger, B. D. 2018, *ApJL*, 868, L4
- Margalit, B., Metzger, B. D., & Sironi, L. 2020b, *MNRAS*, 494, 4627
- Metzger, B. D., Berger, E., & Margalit, B. 2017, *ApJ*, 841, 14
- Metzger, B. D., Margalit, B., & Sironi, L. 2019, *MNRAS*, 485, 4091
- Petroff, E., Hessels, J. W. T., & Lorimer, D. R. 2019a, *A&A Rv*, 27, 4
- Petroff, E., Bailes, M., Barr, E. D., et al. 2015, *MNRAS*, 447, 246
- Petroff, E., Barr, E. D., Jameson, A., et al. 2016, *PASA*, 33, e045
- Petroff, E., Oostrum, L. C., Stappers, B. W., et al. 2019b, *MNRAS*, 482, 3109
- Pilia, M., Burgay, M., Possenti, A., et al. 2020, *ApJL*, 896, L40
- Planck Collaboration, Ade, P. A. R., Aghanim, N., et al. 2016, *A&A*, 594, A13
- Platts, E., Prochaska, J. X., & Law, C. J. 2020, *ApJL*, 895, L49
- Platts, E., Weltman, A., Walters, A., et al. 2019, *PhR*, 821, 1
- Plotnikov, I., & Sironi, L. 2019, *MNRAS*, 485, 3816
- Popov, S. B., & Postnov, K. A. 2013, arXiv:1307.4924, arXiv:1307.4924
- Prochaska, J. X., & Zheng, Y. 2019, *MNRAS*, 485, 648
- Ravi, V., Catha, M., D'Addario, L., et al. 2019, *Nature*, 572, 352
- Rest, A., Stubbs, C., Becker, A. C., et al. 2005, *ApJ*, 634, 1103
- Safarzadeh, M., Prochaska, J. X., Heintz, K. E., & Fong, W.-f. 2020, arXiv, 2009.11735
- Schechter, P. L., Mateo, M., & Saha, A. 1993, *PASP*, 105, 1342
- Schlafly, E. F., & Finkbeiner, D. P. 2011, *ApJ*, 737, 103
- Scholz, P., Spitler, L., Hessels, J., et al. 2016, in *AAS/High Energy Astrophysics Division #15, AAS/High Energy Astrophysics Division*, 105.03
- Scholz, P., Cook, A., Cruces, M., et al. 2020, *ApJ*, 901, 165
- Shannon, R. M., & Ravi, V. 2017, *ApJL*, 837, L22
- Shannon, R. M., Macquart, J. P., Bannister, K. W., et al. 2018, *Nature*, 562, 386
- Skrutskie, M. F., Cutri, R. M., Stiening, R., et al. 2006, *AJ*, 131, 1163
- Spitler, L. G., Cordes, J. M., Hessels, J. W. T., et al. 2014, *ApJ*, 790, 101

- Spitler, L. G., Scholz, P., Hessels, J. W. T., et al. 2016, *Nature*, 531, 202
- Stritzinger, M. D., Taddia, F., Burns, C. R., et al. 2018, *A&A*, 609, A135
- Tanenbaum, B. S., Zeissig, G. A., & Drake, F. D. 1968, *Science*, 160, 760
- Tavani, M., Verrecchia, F., Casentini, C., et al. 2020, *ApJL*, 893, L42
- Tendulkar, S. P., Gil de Paz, A., Kirichenko, A. Y., et al. 2020, *arXiv e-prints*, arXiv:2011.03257
- Thornton, D., Stappers, B., Bailes, M., et al. 2013, *Science*, 341, 53
- Wadiasingh, Z., & Timokhin, A. 2019, *ApJ*, 879, 4
- Yamasaki, S., Totani, T., & Kawanaka, N. 2016, *MNRAS*, 460, 2875
- Zampieri, L., Burtovoi, A., Fiori, M., et al. 2020, *The Astronomer's Telegram*, 13493, 1